We are IntechOpen,
the world's leading publisher of
Open Access books
Built by scientists, for scientists

**4,800**

Open access books available

**122,000**

International authors and editors

**135M**

Downloads

Our authors are among the

**154**

Countries delivered to

**TOP 1%**

most cited scientists

**12.2%**

Contributors from top 500 universities

CLARIVATE ANALYTICS

**BOOK CITATION INDEX**

INDEXED

**WEB OF SCIENCE**™

Selection of our books indexed in the Book Citation Index
in Web of Science™ Core Collection (BKCI)

Interested in publishing with us?
Contact book.department@intechopen.com

Numbers displayed above are based on latest data collected.
For more information visit www.intechopen.com

# Thermodynamics of Nanoparticle Formation in Laser Ablation

Toshio Takiya[1], Min Han[2] and Minoru Yaga[3]
*[1]Hitachi Zosen Corporation*
*[2]Nanjing University*
*[3]University of the Ryukyus*
*[1,3]Japan*
*[2]China*

## 1. Introduction

Nanometer-sized particles, or nanoparticles, are smaller than conventional solid-state materials and possess great potential for new, useful properties due to peculiar quantum effects (Roco, M. C., 1998). Highly functional devices synthesized from nanoparticles have been studied for use in various fields, such as semiconductors (Liqiang, J., 2003; Lu, M., 2006), photocatalysis (Liqiang, J., 2004), secondary batteries (Ito, S., 2005; Kim, K., 2009, 2010), superconductors (Strickland, N. M., 2008), and bonding substances (Ide, E., 2005). In the present chapter, we discuss the thermodynamics related to nanoparticle formation.

Cooling processes of expanding vapor evaporated from a solid surface, such as gas evaporation, arc discharge, sputtering, pulsed microplasma and pulsed laser ablation (PLA), have been applied as a method of nanoparticle formation in the gaseous phase (Wegner, K., 2006). The PLA method, under reduced atmospheric pressure, has been found to be especially promising since it provides the following capabilities (Chrisey, D. B., 1994): (i) ablation of target material regardless of melting point due to the high intensity and focused laser beam pulse, (ii) flexibility in choice of atmospheric gaseous species and pressure, (iii) ease of production of the non-equilibrium state of the high-pressure field due to the formation of shock waves, (iv) ability to obtain many different structured materials, from thin films to micrometer-sized particles, by controlling vapor association and condensation, and (v) ease of synthesis of nano-compounds of non-stoichiometric composition by preparing target materials with desired compositional ratios. The PLA method has been widely used for nanoparticle formation because the formed nanoparticles have diameters smaller than 10 nm with low size dispersion and can be formed as basic materials for highly functional devices via effective utilization of these capabilities (Li, S., 1998; Li, Q., 1999; Patrone, L., 1999, 2000; Wu, H. P., 2000; Suzuki, N., 2001; Inada, M., 2003; Seto, T., 2006).

To understand the process of nanoparticle formation by the PLA method, two perspectives are necessary: (i) the thermodynamics of the microscopic processes associated with the nucleation and growth of nanoparticles, and (ii) the thermodynamics of the macroscopic processes associated with the laser irradiated surface of the target supplying the raw

gaseous materials, combined with the surrounding atmosphere, to provide adequate conditions for nucleation and subsequent growth.

Due to its importance in both academia and industry, the chemical thermodynamics of nanoparticle formation in the gaseous phase have been studied extensively (Finney, E. E., 2008). Two processes are important in these studies: (i) homogeneous nucleation, whereby vapors generated in the PLA process reach super-saturation and undergo rapid phase change, and (ii) growth, during which the nanoparticles continue to grow by capturing surrounding atoms and nuclei in the vapor. The size and generation rate of critical nuclei are important factors for understanding the homogeneous nucleation process. To evaluate the generation rate of critical nuclei, we need to know the partition function of each size of nuclei. If an assembled mass of each size of nuclei can be regarded as a perfect gas, then the partition functions can be calculated using statistical thermodynamic methods. However, because it is generally difficult to directly calculate the nucleus partition function and incorporate the calculated results into continuous fluid dynamics equations, what has been used in practice is the so-called surface free energy model, in which the Gibbs free energy of the nanoparticles is represented by the chemical potential and surface free energy of the bulk materials. In contrast, a kinetic theory has been used for treating the mutual interference following nucleation, such as nanoparticle condensation, evaporation, aggregation, coalescence, and collapse, in the nanoparticle growth process.

Since statistical thermodynamics is a valid approach for understanding the mechanisms of nanoparticle formation, microscopic studies have increased aggressively in recent years. In the case of using a deposition process of nanoparticles for thin-film fabrication for industrial use, however, it is necessary to optimize the process by regulating the whole flow field of nanoparticle formation. In cases in which several vapors (plumes) generated during laser ablation are identified as a continuous fluid, macroscopic studies are needed using, for example, continuous fluid dynamics with a classical nucleation model.

Some studies have evaluated the thermodynamics and fluid dynamics that are involved in nanoparticle formation by using tools such as numerical analysis with an evaporation model, a blast wave model, and a plasma model. However, the shock waves generated in the early stage of PLA result in extensive reflection and diffraction which increasingly complicate clarification of the nanoparticle formation process. Up to now, no attempt to introduce shock wave generation and reflection into the plume dynamics has been reported in relation to nanoparticle formation. We note in particular that thermodynamic confinement could occur at the points of interference between the shock wave and the plume, and that nanoparticles with uniform thermodynamic state variables subsequently could be formed in the confinement region, thus making such a system a new type of nanoparticle generator.

In Section 2 of the present chapter, we review the thermodynamics and fluid dynamics of nanoparticle formation during PLA. After providing analytical methods and models of 1D flow calculation in Section 3, we present the calculation results for laser-irradiated material surfaces, sudden evaporation from the surfaces, Knudsen layer formation, plume progression, and shock wave generation, propagation, and reflection. Extensive 2D flow calculation results (without nanoparticle formation) are presented in Section 4 to explore the flow patterns inside the new type of nanoparticle generator. The experimental results for the various nanoparticles formed by the generator are presented in Section 5. Finally, conclusions are given in Section 6.

## 2. Thermodynamics of nanoparticle formation

### 2.1 Nucleation and growth of nanoparticles

In nanoparticle formation, the following stages must be considered: (i) homogeneous nucleation, where vapor atoms produced by laser ablation have been supersaturated, and (ii) particle growth, where the critical nuclei are growing, capturing atoms on their surfaces, and making the transition into large particles.

At the first stage of homogeneous nucleation, the nucleation rate and the size of critical nuclei are important factors. The nucleation rate, $I$, is the number of nuclei that are created per unit volume per unit time. To evaluate the nucleation rate, the number density of nanoparticles at equilibrium is needed. In the present case, it is assumed that the nanoparticles are grown only in the capture of a single molecule without causing other nuclei to collapse. That is, when a nanoparticle consisting of $i$ atoms is indicated by $A_i$ (hereinafter, $i$-particle), the reaction process related to the nanoparticle formation is expressed as follows:

$$
\begin{aligned}
A_1 + A_1 &\leftrightarrow A_2 \\
A_2 + A_1 &\leftrightarrow A_3 \\
&\ldots\ldots\ldots\ldots \\
A_{i-1} + A_1 &\leftrightarrow A_i
\end{aligned}
\tag{1}
$$

If the molecular partition functions of the various sizes of nanoparticle are derived by statistical mechanical procedure, the equilibrium constants for each equation are known. As a result, the number density of the nanoparticles at equilibrium can be inferred assuming ideal gas behavior. Namely, the equilibrium constant $K_{i-1,i}$ between $(i-1)$-particle and $i$-particle is

$$
K_{i-1,i} = \frac{Q_i}{Q_{i-1}Q_1} \exp\left(\frac{D_{i-1,i}}{kT}\right)
\tag{2}
$$

Here, $Q_i$ is the $i$-particle partition function, $D_{i-1,i}$ is the dissociation energy of one atom for the $i$-particle, $k$ is the Boltzmann constant, and $T$ is the temperature of the system. In general, to explicitly calculate the Gibbs' free energy change from the molecular partition function of nanoparticles and to incorporate these into a continuous fluid dynamics equation are extremely difficult. Therefore, the so-called surface free energy model, where Gibbs' free energy change is represented by the surface tension and chemical potential of bulk materials, can be adopted. Furthermore, when assuming a steady reaction process for nanoparticle formation, the critical nucleation rate, $I$, is represented as (Volmer, M., 1939)

$$
I = \frac{n^2 c v_c}{4 r_*} \sqrt{\frac{3 W_*}{\pi kT}} \exp\left(-\frac{W_*}{kT}\right)
\tag{3}
$$

where $n$ is the number density of species in the vapor, $c$ is the average relative speed between nanoparticles and atomic vapor, $v_c$ is the volume per atom in the vapor, $r_*$ is the radius of the critical nuclei, $W_*$ is the energy of formation for critical nuclei, $k$ is Boltzman constant, and $T$ is the temperature of the system. The exponential term appeared in the above formula seems to be an essential factor for thermodynamic considerations in

nucleation process. The supersaturation, $S$, which is implicitly included in the variable $W_*$, is a dominant factor which significantly affects nucleation rate, $I$.

Once the Gibbs' free energy change, $G$, is known, the critical nucleus radius, $r_*$, can be easily obtained. For this, an assumption of capillary phenomena (capillarity assumption) is used as a condition for mechanical equilibrium of the particles and the extreme value at $dG=0$ may be considered. When the surface tension of the nanoparticle is depicted by σ, the radius of critical nucleus is

$$r_* = \frac{2\sigma v_c}{kT \ln S} \tag{4}$$

Here, as in the case of nucleation rate, the degree of supersaturation, $S$, is what determines the size of the critical nucleus.

Next, it was assumed for convenience that the nanoparticle growth first occurred after its nucleus reached the critical nucleus size. In other words, the Gibbs' free energy of nanoparticle formation begins to decrease after it reaches maximum value at the critical nucleus size. At this time, the number of atomic vapor species condensing per unit area of particle surface per unit time, $\beta$, can be determined using the number density, $N_r$, of the species in the atomic vapor near the surface of a nanoparticle possessing radius, $r$, and assuming the equilibrium Maxwell-Boltzman distribution,

$$\beta = \xi N_r \sqrt{\frac{kT}{2\pi m}} \tag{5}$$

Here, $\xi$ is the condensation coefficient, which represents the ratio of the number of condensing atoms to colliding atoms, and $m$ is the mass of the vapor species. When the vapor species are in equilibrium with the nanoparticles, the number density is represented by $N_{r,eq}$ and the number of atoms evaporating, $a$, from the nanoparticle surface per unit time and area is given by

$$\alpha = \xi N_{r,eq} \sqrt{\frac{kT}{2\pi m}} \tag{6}$$

Therefore, the growth rate of the nanoparticle radius is

$$\frac{dr}{dt} = (\beta - \alpha) v_c \tag{7}$$

In this equation, the variable $a$ is the equilibrium value corresponding to the temperature of the nanoparticle, while the kinetic parameters of the surrounding vapors, which affect significantly the variable $\beta$, are dominant.

As mentioned above, when the two processes of nanoparticle nucleation and growth are considered, each parameter governing the processes is different. That is, the degree of supersaturation dominates as a non-equilibrium thermodynamic parameter for nucleation, while the state variables related to the surrounding vapors are important as molecular kinetic parameters for particle growth. Thus, separating the nucleation and growth processes in time by using the difference, could hypothetically lead to the formation of nanoparticles of uniform size.

## 2.2 Thermal analysis and Knudsen layer analysis

In the view of gas dynamics, the PLA process can be classified into (i) evaporation of the target material and (ii) hydrodynamic expansion of the ablated plume into the ambient gas. We make the approximation herein of a pure thermal evaporation process and neglect the interaction between the evaporated plume and the incident laser beam. For the fairly short laser pulses (~10 ns) that are typical for PLA experiments, it is reasonable to consider the above two processes as adjacent stages. The energy of the laser irradiation is spent heating, melting, and evaporating the target material. The surface temperature of the target can be computed using the heat flow equation (Houle, F. A., 1998). For very high laser fluences, the surface temperature approaches the maximum rapidly during the initial few nanoseconds of the pulse. The evaporation process becomes important when the surface temperature of target approaches the melting point. With the laser fluence and pulse duration we considered, thermally activated surface vaporization can reasonably be used to describe the evaporation due to pulsed laser irradiation of the target. The saturated vapor pressure, $p_v$, in equilibrium at the target surface can be calculated using the Clausius–Clapeyron equation from the surface temperature, $T_s$. The flux of vapor atoms leaving the surface can be written as

$$J = \frac{\eta p_v}{\sqrt{2\pi k T_s m}} \tag{8}$$

where $\eta$ ($\approx 1$) denotes the sticking coefficient of surface atoms and $m$ is the atomic mass of the vapor atom. The total number of ablated atoms is an integration of $J$ over time and surface area.

To obtain the initial condition for vapor expansion problem, we can perform a Knudsen layer analysis to get the idealized states of the gas just leaving the Knudsen layer (Knight, C. J., 1979). The local density, $n_0$, mean velocity, $u_0$, and temperature, $T_0$, of the vapor just outside the Knudsen layer can be calculated from the jump conditions and may be deduced very simply using

$$\frac{T_0}{T_s} = \left[ \sqrt{1 + \pi \left(\frac{g}{8}\right)^2} - \sqrt{\pi}\frac{g}{8} \right]^2 \tag{9}$$

$$\frac{n_0}{n_s} = \sqrt{\frac{T_s}{T_0}} \left[ \left(g^2 + \frac{1}{2}\right) e^{g^2} erfc(g) - \frac{g}{\sqrt{\pi}} \right] + \frac{1}{2}\frac{T_s}{T_0} \left[ 1 - \sqrt{\pi} g e^{g^2} erfc(g) \right] \tag{10}$$

$$u_0 = \sqrt{\kappa \frac{k T_0}{m}} \tag{11}$$

where $n_s$ is the saturated vapor density at the target surface g is a function of Mach number and $\kappa$ is the adiabatic index. The idealized states just beyond the Knudsen layer are calculated by using the above equations (Han, M., 2002).

## 3. One dimensional flow problems

### 3.1 Fluid dynamics of laser ablated plume

Since the processes described above for nanoparticle formation arise in the high temperature plume generated by laser ablation, it is important to know the thermodynamic state of the

species in the plume. The one-dimensional unsteady Euler compressible fluid equation can be obtained using the numerical scheme in order to solve the thermodynamic state of the plume species, as well as to understand the nanoparticle nucleation and growth. Discretization of the system equation was driven by a finite volume method in which a total variation diminishing (TVD) scheme for capturing the shock wave was adopted as a numerical viscosity term. In the present study, because the time evolution of the plume and shock wave interference need to be considered, a three-order precision Runge-Kutta scheme was used as the accurate time calculation.

The conservation equations of mass, momentum, and energy, which describe the behavior of the laser plume in an ambient gas, are as follows (Shapiro, A. H., 1953),

$$\frac{\partial \mathbf{Q}}{\partial t} + \frac{\partial \mathbf{E}}{\partial x} = \mathbf{W} \tag{12}$$

where

$$\mathbf{Q} = \begin{bmatrix} \rho_v & \rho_g & \rho_m u & e & C_1 & C_2 & C_3 & C_4 \end{bmatrix}^{\mathrm{T}} \tag{13}$$

$$\mathbf{E} = \begin{bmatrix} \rho_v u & \rho_g u & p + \rho_m u^2 & (e+p)u & C_1 u & C_2 u & C_3 u & C_4 u \end{bmatrix}^{\mathrm{T}} \tag{14}$$

$$\mathbf{W} = \begin{bmatrix} -\dot{\rho}_c & 0 & 0 & \lambda \dot{\rho}_c & I & \dot{r}C_1 & 2\dot{r}C_3 & 4\pi \dot{r}C_3 \end{bmatrix}^{\mathrm{T}} \tag{15}$$

Here, $x$ and $t$ are distance and time, respectively, and the variables $\rho$, $u$, $p$ and $e$ are the density, velocity, pressure, and the total energy per unit volume, respectively. The sub-indices for the vapor, the ambient gas, and the gas mixture are expressed respectively as $v$, $g$ and $m$. Moreover, $\lambda$ is latent heat for the bulk material of the naonoparticle. In addition, the dotted variables $\dot{\rho}$ and $\dot{r}$ represent the time derivative related to the density and the radius of nanoparticle, respectively. $C_1$, $C_2$, $C_3$, and $C_4$ are transient intermediate variables; among these, the last variable, $C_4$, also represents the nanoparticle density, $\rho_c$.

## 3.2 Calculation model for 1D flow

Figure 1 shows a numerical calculation model of nanoparticle formation during laser ablation. The one-dimensional computational domain, also called the confined space in the present study, is surrounded by a solid wall on the left and a laser target on the right (Takiya, T., 2007, 2010). The confined space is initially filled with ambient gas. The figure represents the initial state of the flow field immediately after laser irradiation. The target surface is melted by laser irradiation and then saturated vapor of high temperature and pressure is present near the surface. Outside it, the Knudsen layer, the non-equilibrium thermodynamic region where Maxwell-Boltzmann velocity distribution is not at equilibrium, appears. Following the Knudsen layer is the initial plume expansion, which is the equilibrium thermodynamic process. In this case, the high temperature and high pressure vapor, which is assumed to be in thermodynamic equilibrium, is on the outer side of the Knudsen layer and is given as the initial conditions for a shock tube problem. In the calculation, the high temperature and high pressure vapor is suddenly expanded, and a

plume is formed forward. With the expansion of the plume, the ambient gas that originally filled the space is pushed away to the right and towards the solid wall.
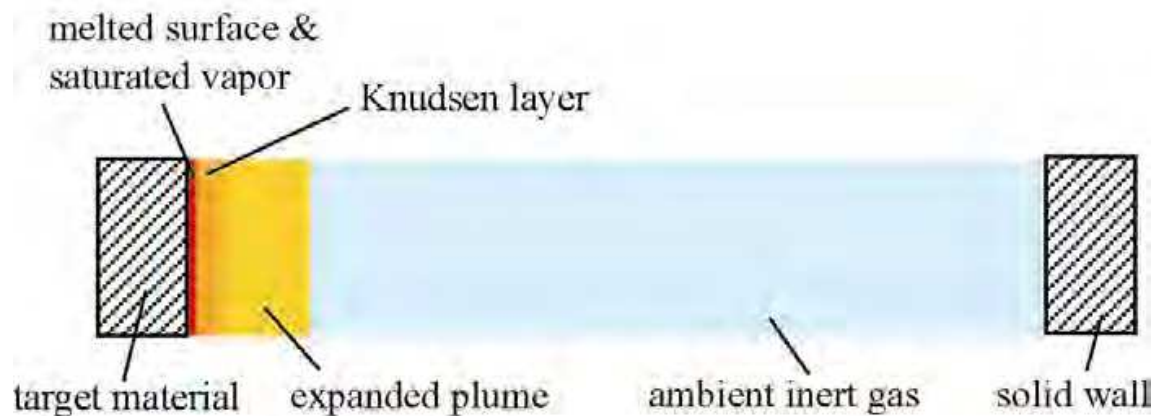


Fig. 1. Calculation model for 1D flow

### 3.3 Physical values and conditions

In this calculation, Si was selected as the target for laser ablation. Physical properties of Si used in the calculations are shown in Table 1 (Weast, R. C., 1965; Touloukian, Y. S., 1967; AIST Home Page, 2006).

As parameters in the simulation, the atmospheric gas pressure, $P_{atm}$, and target-wall distance, $L_{TS}$, may be varied, but conditions of $P_{atm}$ = 100 Pa and $L_{TS}$ = 20 mm were most commonly used in the present study. To examine the confinement effect on the nanoparticle formation, however, parametric numerical experiments for $L_{TS}$ = 20, 40, 60, 80, and 200 mm were also conducted.

| | |
|---|---|
| Thermal conductivity at 300K | 156 [W/(m·K)] |
| Density | 2330 [kg/m³] |
| Thermal capacity at 298K | 712 [J/(kg·K)] |
| Melting enthalpy | 1.804 [kJ/g] |
| Vaporization enthalpy at 1550K | 15.67 [kJ/g] |
| Melting point | 1683 [K] |
| Boiling point | 2628 [K] |

Table 1. Physical values of Si

The parameters for laser irradiation of the target, the surface, and the vapor conditions are shown in Table 2. Here, the Laser energy is the energy per single laser pulse, the Laser fluence is the energy density of laser beam having a diameter of 1 mm, the Surface temperature is the temperature of the target surface resulting from the thermal analysis, and the Vapor temperature and Vapor density at the Knudsen layer are the conditions resulting from the Knudsen layer analysis.

| Laser energy | 20 mJ |
|---|---|
| Laser fluence | 25 mJ / mm$^2$ |
| Surface temperature | 6100 K |
| Temperature at Knudsen layer | 4050 K |
| Vapor density at Knudsen layer | 1.54 kg / m$^3$ |

Table 2. Parameters for laser irradiation

### 3.4 Typical results for 1D flow

To substantially separate the nucleation and the growth of nanoparticles and facilitate the formation of uniform-sized nanoparticles, the behavior of the shock wave incidentally generated by laser ablation was investigated.

Nanoparticle evaporation is generally thought to be due to an increase in temperature during the passage of shock waves. Therefore, comparatively weak shock waves, which occur in soft laser ablation, were used to promote nanoparticle growth without the evaporation. When soft laser ablation in the confined space was studied, the shock wave and plume were generated, followed by the collision of the reflected shock wave into the plume front. For verification of these processes, a simulation was also carried out with the one-dimensional compressible fluid equations.

A typical flow profile in the calculation showing the change in densities of the Si vapor, helium gas, and nanoparticles between the target surface and the solid wall are shown in Figure 2. Figure 2(a) indicates these densities in the early stages following laser ablation. In general, the silicon vapor atoms in the plume generated by laser ablation are in the electronically excited state by the high energy of the laser. In the plume front, an emission has been observed with de-excitation based on collisions between the vapor atoms and helium gas. Pushing away helium gas by expansion, the plume gradually increases the density in the front region by reaction. Because the ablation laser pulse is limited to a very short time duration, the plume cannot continue to push away helium gas. The clustering of atomic vapors can thus be promoted in the compressed region of plume due to an increase in supersaturation. In front of the plume, it is clearly shown that a shock wave is formed and propagated in helium gas. A transition is observed wherein the plume propagation speed is greater than the speed of the shock wave (Figures 2(b) to 2(d)). On the other hand, while the peak height of plume density progressively decreases, the spatial density of the nanoparticles continues to increase. The shock wave crashes into the right side wall and reflects to the left (Figures 2(e) and 2(f)). In addition, the peak position of nanoparticle density is slightly shifted from the peak position of vapor density. The shock wave is strengthened by reflection to the right side wall, followed by collision with the plume (Figure 2(g)). Figure 2(h) shows the state just after the collision between the reflected shock wave and the plume. The shock wave penetrates into the plume, enhanced the plume density, and thus slightly pushes it back to the left (Figure 2(i)). When the shock wave has completely passed through the plume, the spatial density of nanoparticles effectively increases(Figure 2(j)).
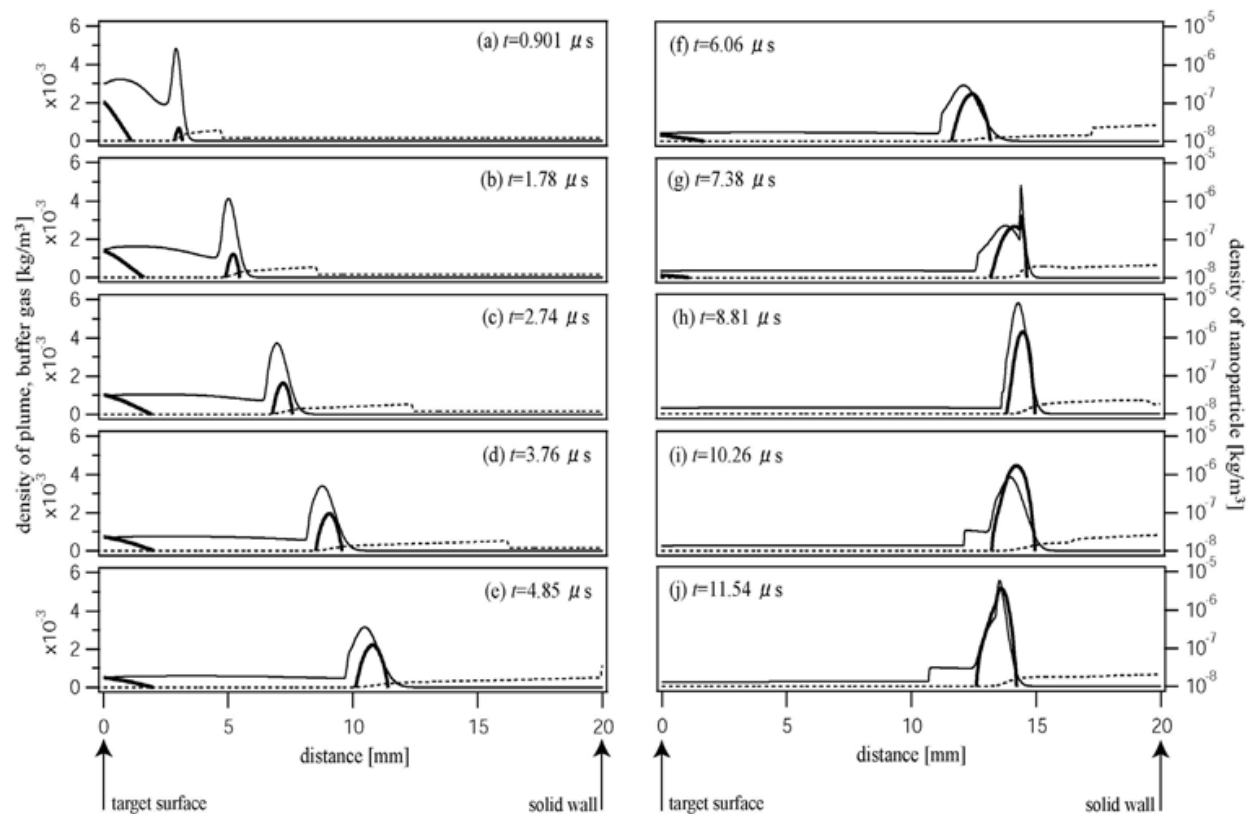
Fig. 2. Typical flow field calculated using the methods and conditions presented in Section 3.3.

### 3.5 Nucleation and growth

Using the same conditions as discussed in the previous section, more detail on the time variation of the state variables is presented in this section.

Figure 3 (a) shows the time variation of the total mass of nanoparticles in the confined space. The horizontal axis is the elapsed time from laser irradiation. This axis is logarithmic to facilitate simultaneous description of the multiple phenomena occurring over several different time scales. The mass of nanoparticles increases between 0.001 µs and 0.1 µs (Figure 3(a)). After 0.1 µs, the mass becomes constant and begins to rise again at 10 µs. The time of the second mass increase is consistent with the moment at which the reflected shock wave collides with the plume. The time variation of the spatially averaged nucleation rate in the confined space is shown in Figure 3(b). The nucleation rate reaches a maximum value at 0.01 µs. The integrated value of nucleation also increases rapidly in the early stages and then becomes constant (Figure 3(c)), which means that the nucleation phenomenon is completed very early on.

The variation of nanoparticle size, which corresponds to the spatially averaged number of atoms constructing the nanoparticle, is shown in Figure 3(d). Since the nanoparticle size starts to increase at 10 µs, when the reflected shock wave arrives at the plume front, it substantially determines the final nanoparticle size, which indicates that the growth of the nanoparticles is facilitated by the effect of the reflected shock wave. Because the nucleation is completed at a very early stage, as already shown, the calculated results also show that nanoparticle growth can be clearly separated from the nucleation process.
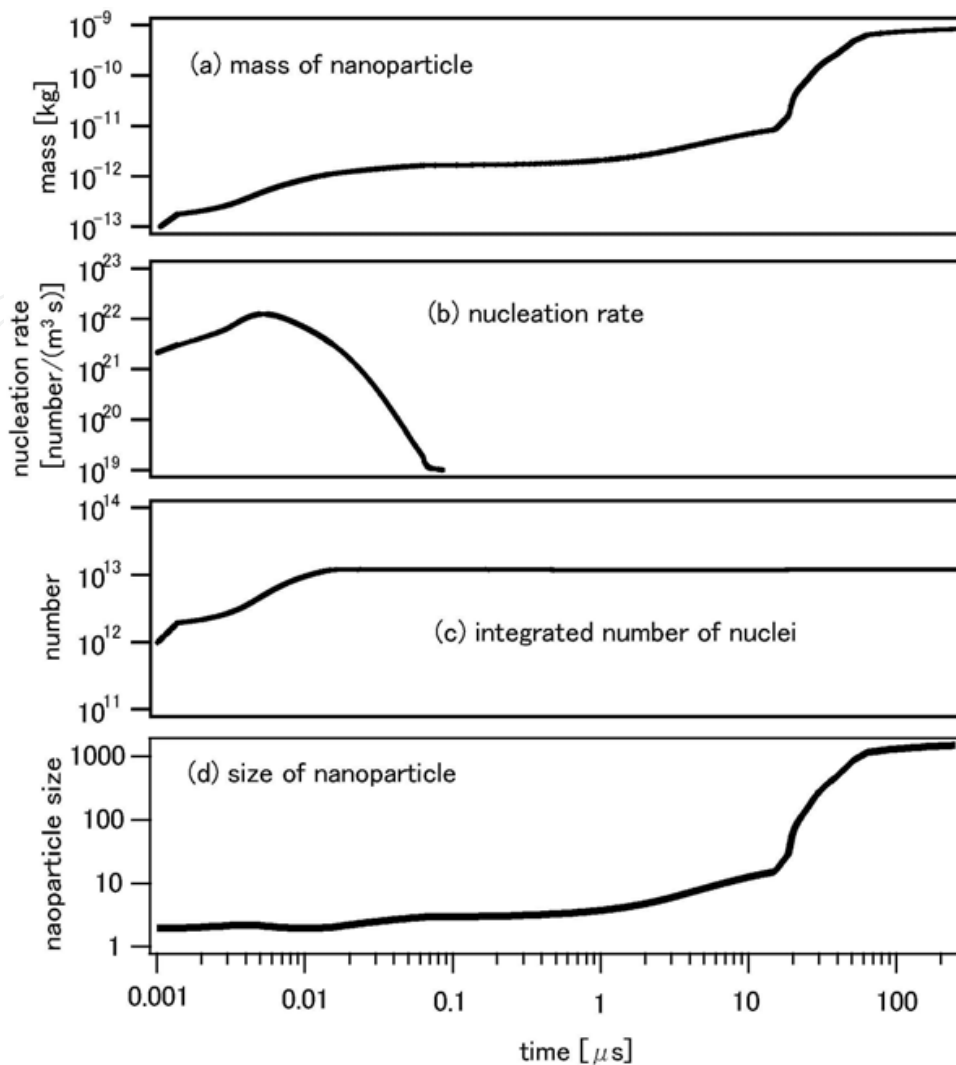
Fig. 3. Time variation of nucleation and growth of nanoparticles

### 3.6 Influence of confinement

The change in nanoparticle size over time was also examined; nanoparticle size increased when the shock wave hit the plume front. Before examining this process further, however, the typical nanoparticle size, as well as the locations of the plume front and the shock wave, must be clearly defined.

There is a definite relationship between the size and spatial density of nanoparticles. The nanoparticle size generally has a distribution, which is especially large in the region of the plume front. The width of the nanoparticle density distribution is smaller than the spread in nanoparticle size and has a sharper distribution profile. The peak positions of the two distributions are almost identical. This means that the maximum nanoparticle size is placed at the location where the nanoparticle density is also at a maximum. Therefore, the typical nanoparticle size in the space can be regarded as the maximum nanoparticle size.

The location of the shock wave propagating through the ambient gas is defined as the maximum value of the derivative for the change in gas density. On the other hand, the plume front is defined as the compression region in the atomic vapor, which comes into contact with the atmospheric gas and high-density area.

The time variation of the nanoparticle size and the positions of the shock wave and the plume, which were defined above, are shown in Figure 4. The left vertical axis is the nanoparticle radius, the right vertical axis is the position in the calculation region, and the horizontal axis is the elapsed time from laser irradiation. The dashed line, thick solid line, and the shaded area represent the nanoparticle size, the position of the shock wave, and the plume front, respectively. The shock waves are propagated backward and forward in the space by reflecting on the target surface and the opposed wall. The width of the shaded area, which represents the plume front, gradually broadens. In addition, the first, $Tc_1$, and second, $Tc_2$, times when the shock wave interferes with the plume front are shown. This interference can be seen as opportunities to enhance the growth rate of nanoparticles. The slope of the dashed line in Figure 4 represents the nanoparticle growth rate, which changes from 17.5 to 52.0 µm/s at $Tc_1$, and from 16.0 to 34.2 µm/s at $Tc_2$. Referring back to Eq. (7), the growth rate of the nanoparticles was determined by a kinetic balance between the condensation rate of nanoparticles, which is based on a macroscopic collision cross-section of the ambient vapors, and the evaporation rate of nanoparticles corresponding to the nanoparticle temperature. Therefore, the fact that the nanoparticle growth rate increases when the shock wave and plume collide means that the shock wave effectively increases the macroscopic collision cross-section.
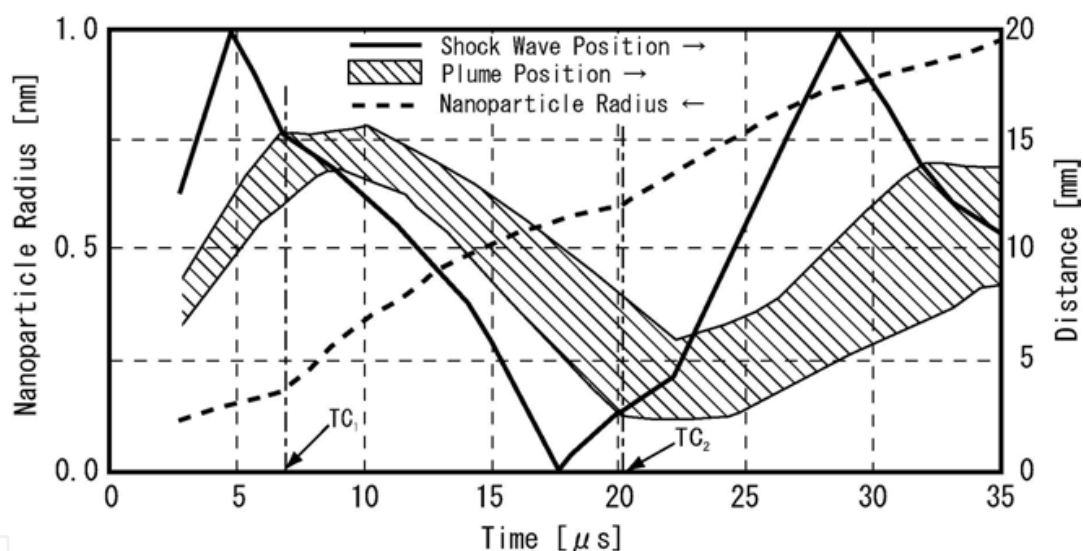


Fig. 4. Increase of nanoparticle radius from interference between shock wave and plume

To investigate the effect of the distance between the target surface and the solid wall on the rate of nanoparticle growth enhanced by the shock wave passage, the numerical simulation was performed under the following conditions: $L_{TS}$ = 20, 40, 60, 80, and 200 mm. The calculated results for the increase of nanoparticle radius are indicated in Figure 5 against the elapsed time from laser irradiation. Nanoparticle growth was promoted by the passage of the shock wave under all of these conditions. The nanoparticle radius, $r$, increased with time and eventually reaches a constant value. A balance between the evaporation rate and condensation rate is reached at the maximum radius, and the growth rate of nanoparticles asymptotically approaches zero. When the radius of the nanoparticle is compared among the various distances between the target surface and the solid wall, the shorter $L_{TS}$ resulted in a larger value of $r$. Therefore, larger nanoparticles can be obtained with smaller distances because there are more opportunities for the shock waves to pass through the plume front before the condensation rate balances the evaporation rate.
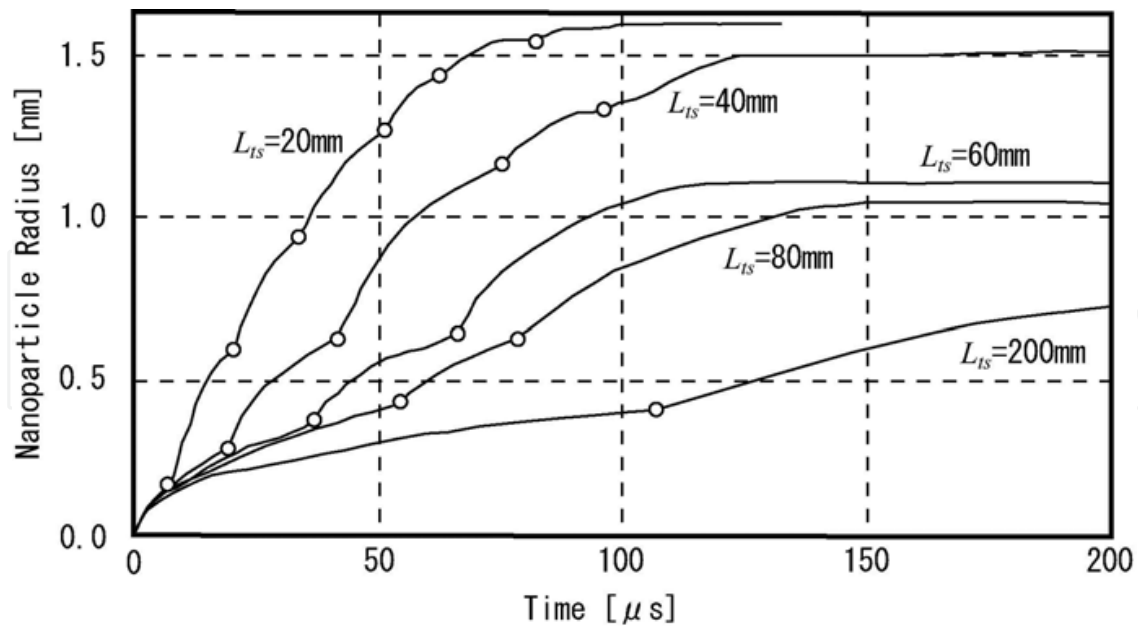
Fig. 5. Influence of distance between target and wall on nanoparticle growth. The circles indicate the arrival time of the shock wave.

## 4. Two dimensional flow problem

### 4.1 Calculation model for 2D flow

On the basis of the results described in the previous section, we have proposed a new method for the direct generation of monodisperse nanoparticles. This method makes use of interaction phenomena between the plume and shock wave arising in an ellipsoidal cell following laser ablation in ambient gas. The method is based on the hypothesis that monodisperse nanoparticles are instantaneously formed inside a narrow region constructed from a diffusion mixture of vapor and ambient gas during the interaction between a plume and shock wave. Such a region forms at one focal point of the ellipsoidal cell, while the plume is ejected from the other focal point with laser irradiation being accompanied by shock waves. Here, the ellipsoidal cell is used as an experimental device based on this principle to obtain uniformly sized nanoparticles, which does not require an additional size classifier like a differential mobility analyzer (Camata, R. P., 1996), and therefore is expected to show high efficiency (Iwata, Y., 2002).

The basic idea of the proposed device, illustrated in Figure 6, is as follows: the target material is exposed to a high-power pulsed laser; the ablated vapor suddenly expands due to high temperature; the expansion results in a propagating shock wave (Figure 6(a)); the vapor is fed by the ablation process for a period of the exposure of the pulse laser; the plume propagates toward the cell exit (Figure 6(b)); the ablation stops after a short duration, while the shock wave and the plume continue to propagate and start to interact (Figures 6(b) and 6(c)); and after the complex interaction between them, the monodispersed nanoparticles are produced and extracted through the cell exit (Figure 6(d)). During the interaction, it is important for the nanoparticles to grow to a certain size.

To investigate the effect of this new model, 2D calculations were performed. For the governing equations, we have chosen the axisymmetric, two-dimensional, compressible Navier–Stokes equations, because the experiments showed that the laser-ablated plume travels straight toward the cell exit with no distortion. The equations are solved by a finite

volume method using the MUSCL-type total variation diminishing (TVD) scheme with a curvilinear generalized coordinate (Yaga, M., 2005, 2008; Fukuoka, F., 2008)
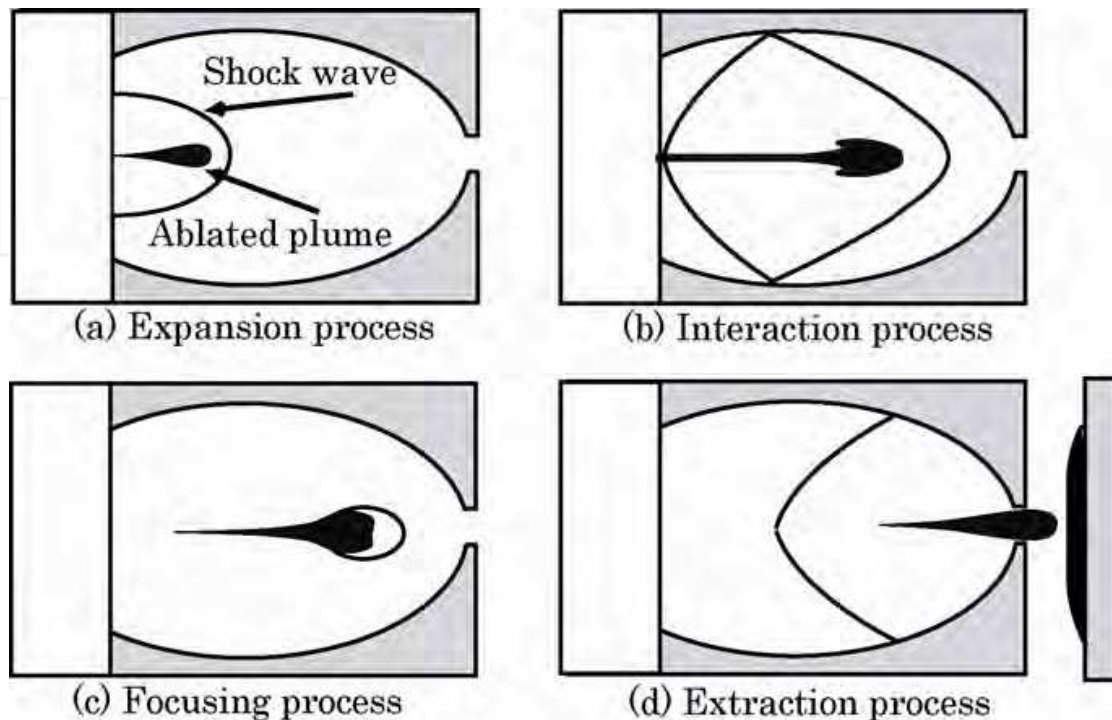


Fig. 6. Behavior of plume and shock wave in an ellipsoidal cell.

**4.2 Boundary and initial conditions**
The contours of the wall are calculated by the following equation:

$$\sqrt{\frac{x^2}{a^2}+\frac{y^2}{b^2}}=1 \qquad (16)$$

where, $a$ and $b$ are constants with a relation of $a=b\left(1+\sqrt{5}\right)/2$.

For the boundary conditions, non-slip conditions are applied to the cell wall, except for the position of the plume ejection. Outgoing flow conditions are applied to the boundaries outside the cell. The position of the plume ejection is set at one of the focal points of the ellipsoidal cell. The sudden ejection generates a traveling shock wave which is converges at the other focal point. The cell exit, through which the flow passes during the propagations of the shock and pressure waves, connects the inside and outside of the cell. During the focusing process of the propagating shock wave, the interaction between the converging shock wave and plume plays an important role in the growing nanoparticle size. An ejected jet of gas is shut off after a certain period so that the calculation can be used for a basic reference for PLA techniques. Then, the ejected gas is considered to be a plume traveling toward the exit of the cell on the right side wall. It is clear that many parameters are involved in this process. We have chosen the three main parameters to be the Mach number, jet duration, and diameter of the exit hole, because, in related experiments, the controllable

parameters are the laser power, duration of the laser pulse, and diameter of the cell exit hole. We therefore assume that the experimental parameters related to the laser power and pulse correspond to the jet Mach number and jet duration, respectively. Hence, we have selected the above three parameters to be tested, fixing all the other parameters. The states of the gas inside and outside of the cell are initially at rest, that is, the ambient properties such as the pressure, density, temperature are uniform over the whole calculation region.



(a) Step 1200  t*= 0.415E+02

(b) Step 2200  t*= 0.764E+02

(c) Step 2600    t*= 0.903E+02

(d) Step 3000  t*= 0.104E+03

(e) Step 3300  t*= 0.114E+03

(f) Step 7900  t*= 0.276E+03
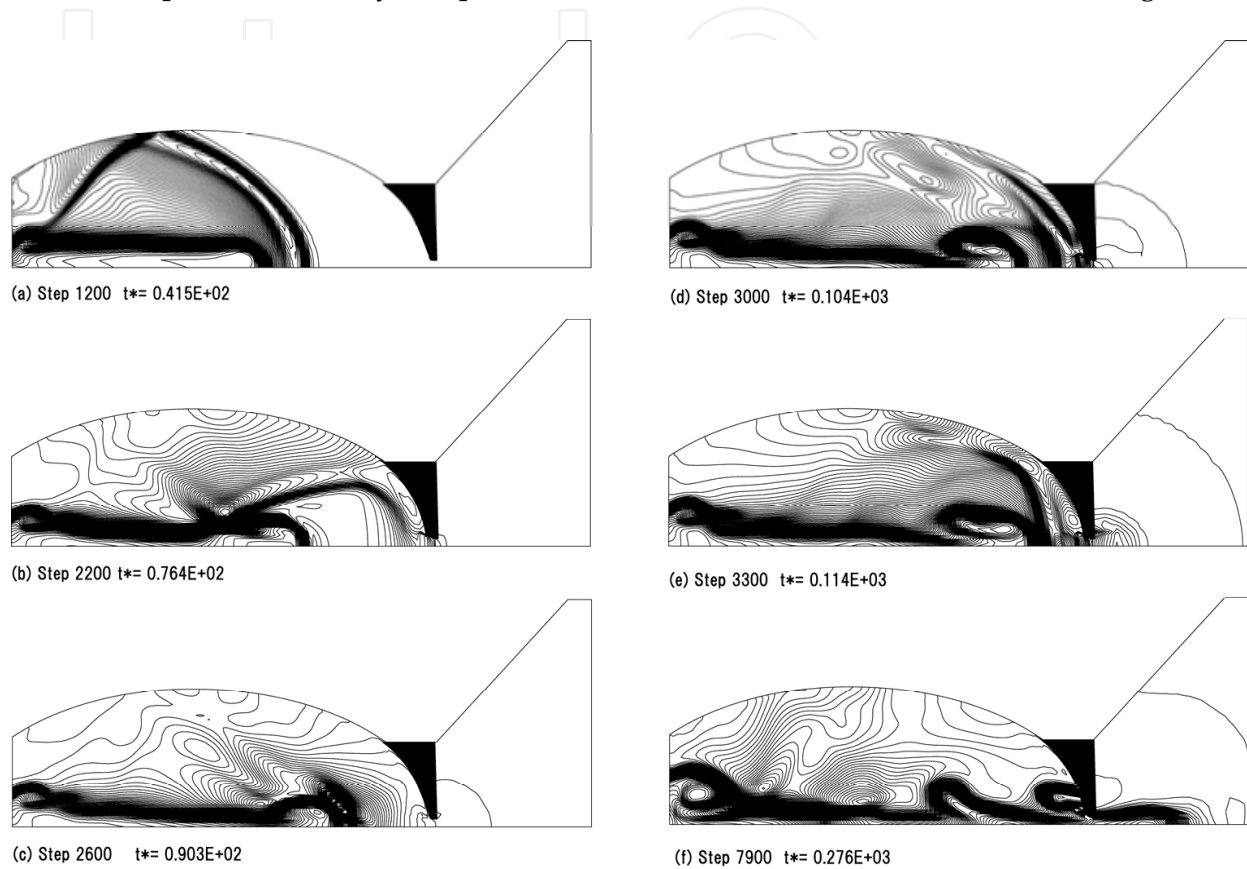
Fig. 7. Time variations of density contours in the ellipsoidal cell.

### 4.3 Shock wave behavior and interaction with plume

Figures 7(a) to (f) show the calculated density fields using certain parameters. As illustrated in the previous section, a shock wave was generated by the sudden expansion of the ejected plume in the ellipsoidal cell. Together with the plume jet, the shock wave propagated towards the right wall of the cell. The plume has decelerated while the shock wave continues to move towards the exit hole (Figure 7(a)). The distance between the plume front and the shock wave increased. The propagating shock wave was reflected from the upper wall of the cell and changed direction toward the focal point. The propagating shock wave arrived at the exit hole and was reflected from the cell wall (Figure 7(b)). The shock wave behind the plume started to interact with the plume front. Figure 7(c) shows the moment when the shock wave was focused at the focal point of the cell and, at the same time, the plume front was located at almost the same point. The plume seems to be blocked by the converging shock wave. Namely, it was recognized that a confinement of the plume was occurred at the time. The transmitted shock wave through the exit hole is so weak that the density contour fields outside of the cell cannot be seen. After the shock wave has

converged at the focal point, it began to spread out again. Most of the spreading shock wave, except for the left traveling shock wave, impinged on the wall again (Figure 7(d)). The shock wave around the exit hole causes weak compression waves to be transmitted into the cell through the hole. After the spreading shock wave was reflected from the wall again (Figure 7(e)), it started to converge at the focal point, where the plume is already present. Then, the shock wave, having been through two reflections, is strong enough to deform the plume and flatten the vortices. The deformed plume front still has enough momentum to transmit through the exit hole (Figure 7(f)). However, part of the plume is left in the cell due to the small diameter of the exit hole. Figure 7(f) suggests that the exit diameter is an important factor in evaluating how much of the plume can get through the exit hole. By choosing the suitable size of exit hole, we can efficiently extract the plume, which once converged at the focal point of the ellipsoidal cell. If these suitable conditions are applied to the actual laser ablation process in the ellipsoidal cell, the laser ablated plume can be confined by a converging shock wave followed by a generation of monodispersed nanoparticles.

## 5. Experimental results

### 5.1 Experimental equipment

The main part of the experimental setup, shown in Figure 8, is composed of the generation and deposition chamber. The laser beam is introduced into the generation chamber. The laser plume is confined by the ellipsoidal cell and uniform-sized nanoparticles are generated. An ambient gas is supplied into the ellipsoidal cell and the cell is filled with the gas. The deposition chamber is connected to the generation chamber through a skimmer, where the nanoparticles are extracted by the ambient gas flow. A substrate is placed in a vertical position for the deposition of the nanoparticles.
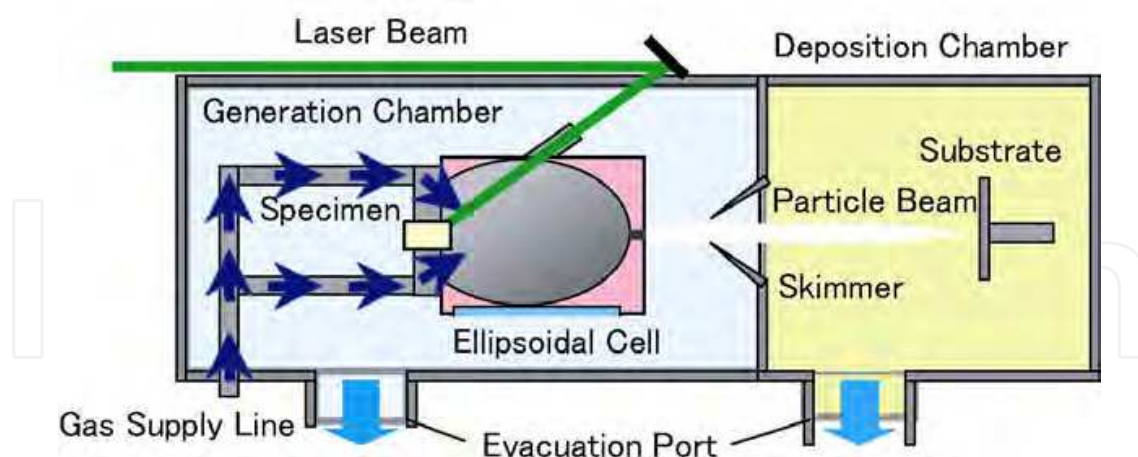


Fig. 8. Schematic diagram of the apparatus for the nanoparticle formation using Pulsed Laser Ablation

When the high-power pulsed laser is directed onto a solid sample in the ellipsoidal cell filled with the ambient gas, the plume is ejected perpendicular to the sample surface. At that time, a shock wave is also generated, driven by the plume expansion, and then propagates in the ambient gas. By placing the sample surface on the focal point of the ellipsoidal cell, the shock wave is reflected on the inner wall of the cell and focused onto the other focal point.

The plume then collides with the ambient gas, which is considerably denser because of the shock wave focusing in the vicinity of this focal point. A mixture region, where the thermodynamic states are uniform, is formed in the boundary between the ambient gas of high density and the plume front and where the mono-disperse nanoparticles are formed.

## 5.2 Typical examples

Experiments were carried out with an ellipsoidal cell having an exit hole diameter of 2 mm, a long axis of 30 mm, and a short axis of 19 mm. An Nd:YAG laser with second harmonic generator ($\lambda$ = 532 nm) was used, and the sample was oxygen-free copper. Helium was chosen as the ambient gas, and the cell pressures were 100, 500, and 1000 Pa. The energy of the laser pulse was 256 mJ, with a pulse duration of 8 ns. The laser irradiated area was measured to be 3.88 mm² from observation of a laser trace on the sample surface.

An image of the copper nanoparticles after 30 laser pulses obtained with transmission electron microscopy (TEM) is shown in Figure 9. Although some grain growth due to aggregation of nanoparticles after generation is recognized in the case of gas pressure 1000 Pa, monodisperse nanoparticles less than 10 nm are easily obtainable by properly controlling the ambient gas pressure.

Nanoparticle size distributions analyzed using TEM with a 0.5 µm square field of vision are shown in Figure 10. Using gas pressures of 100 and 500 Pa, nanoparticles with average diameters below 10 nm were obtained. In both cases, the particle size distribution can be approximated using a lognormal distribution function. The geometric standard deviation, $\sigma$, ranges from 1.09 to 1.12. Furthermore, it was confirmed in other experiments that the standard deviation can be further reduced by reducing the diameter of the exit hole of the ellipsoidal cell.
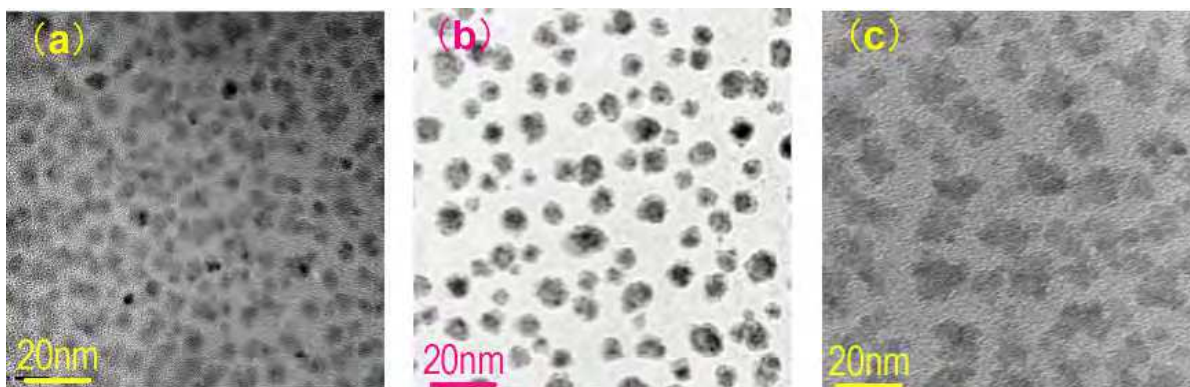


Fig. 9. TEM images of Cu nanoparticles formed under (a)100, (b)500 and (c)1000 Pa of helium gas pressure.

An electron diffraction pattern and corresponding TEM image of copper nanoparticles is shown in Figure 11. By comparing the diffraction pattern of the copper nanoparticles with that of only the carbon film on which the nanoparticles were collected, we confirmed that the copper nanoparticles are as crystalline. Debye Scherrer rings are observed in the electron diffraction pattern where most of Laue spots are very small, suggesting that the crystallized nanoparticles are facing various directions with respect to the nanoparticle crystal axis.
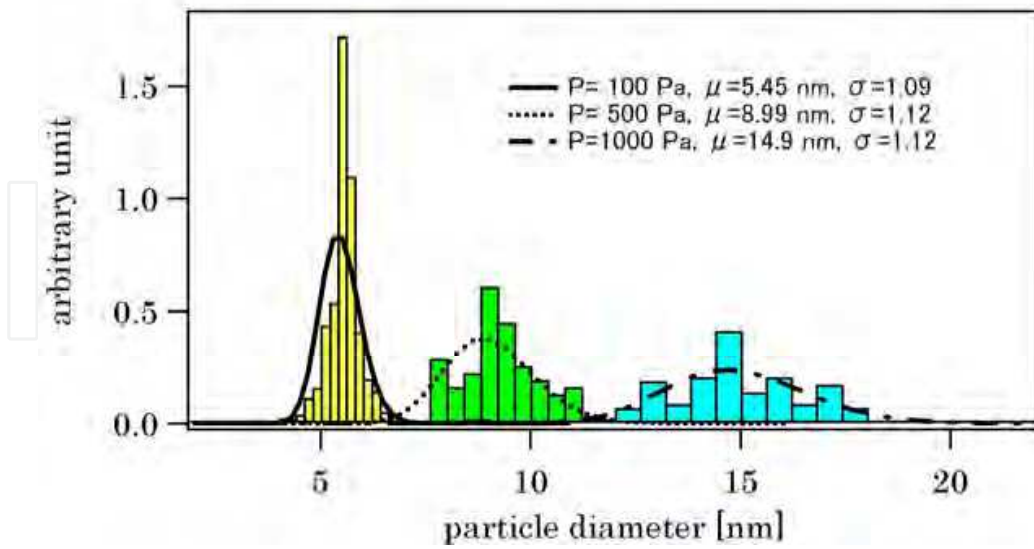
Fig. 10. Histograms showing the diameters and the logarithmic normal distributions of the nanoparticles.
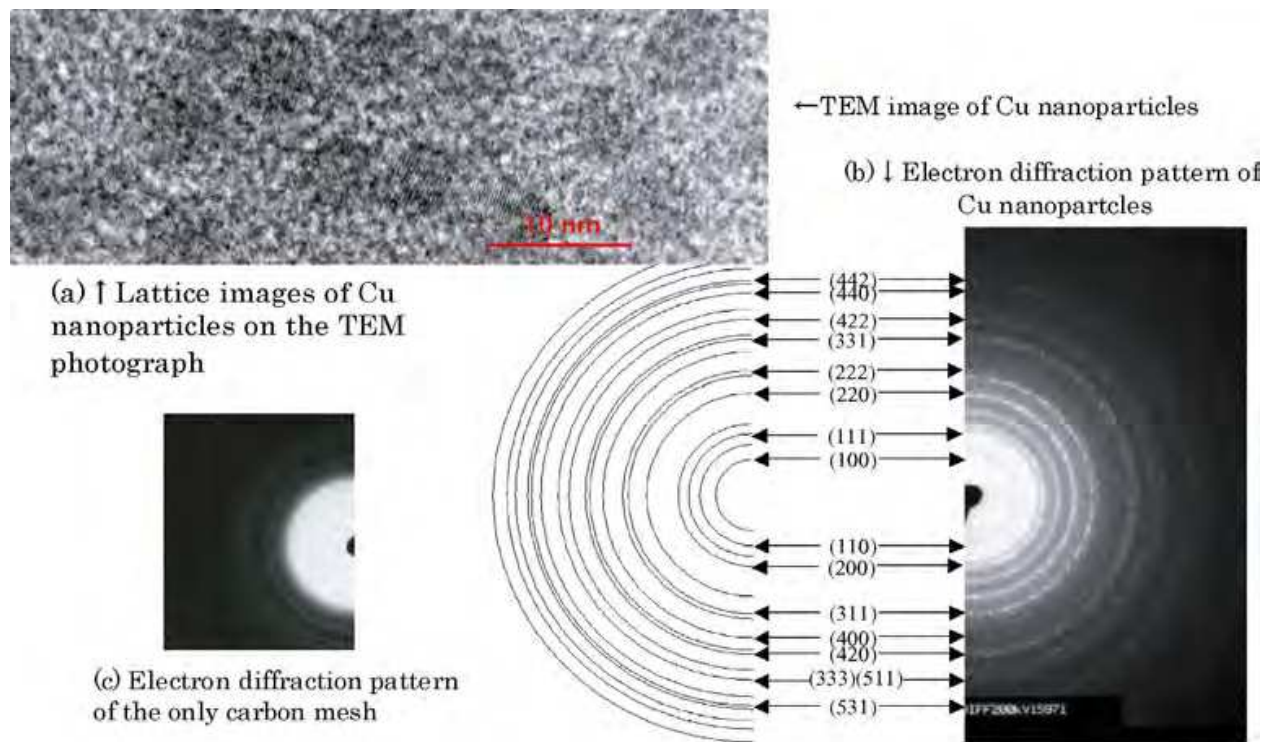


Fig. 11. TEM images and corresponding the electron diffraction patterns of Cu nanoparticles.

## 5.3 Confinement effects

As already stated, in order to produce monodispersed nanoparticles, it is important to confine the plume within the converging shock waves. To confirm the importance of

confining the plume at the focal point of the ellipsoidal cell, further nanoparticle formation experiments were carried out.

Figure 12 is a schematic diagram of the apparatus with an ellipsoidal cell. The laser spot is intentionally shifted by a distance, $x$, from the central axis of the ellipsoidal cell, while the target surface is also intentionally inclined by an angle, $\theta$, against a plane perpendicular to the central axis. Figure 13 shows some of the results for nanoparticles produced as a result of changing these parameters. The experimental results shown in Figure 13(a), which are obtained under the conditions $x = 0.0$ mm and $\theta = 0.0$ °, represent monodispersed nanoparticles. When the target surface has no inclination but the laser spot is shifted $x = 2$
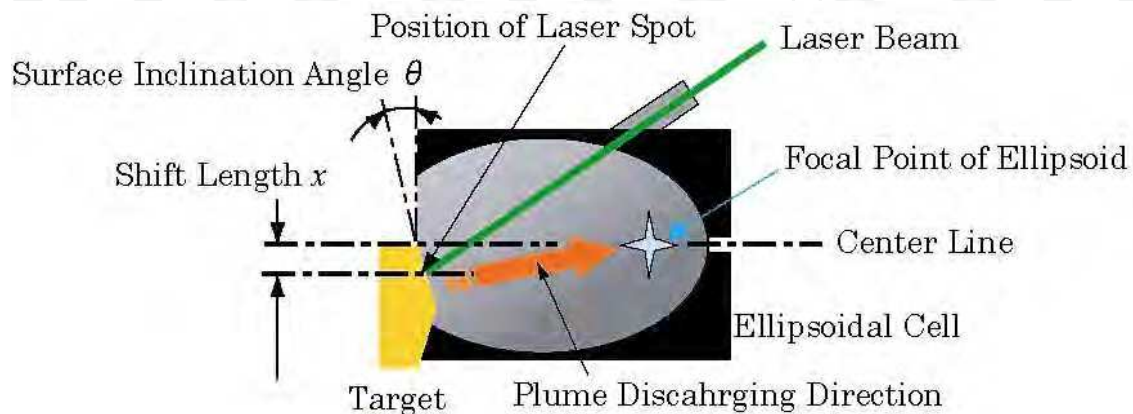
Fig. 12. Schematic of experiment demonstrating the importance of confinement
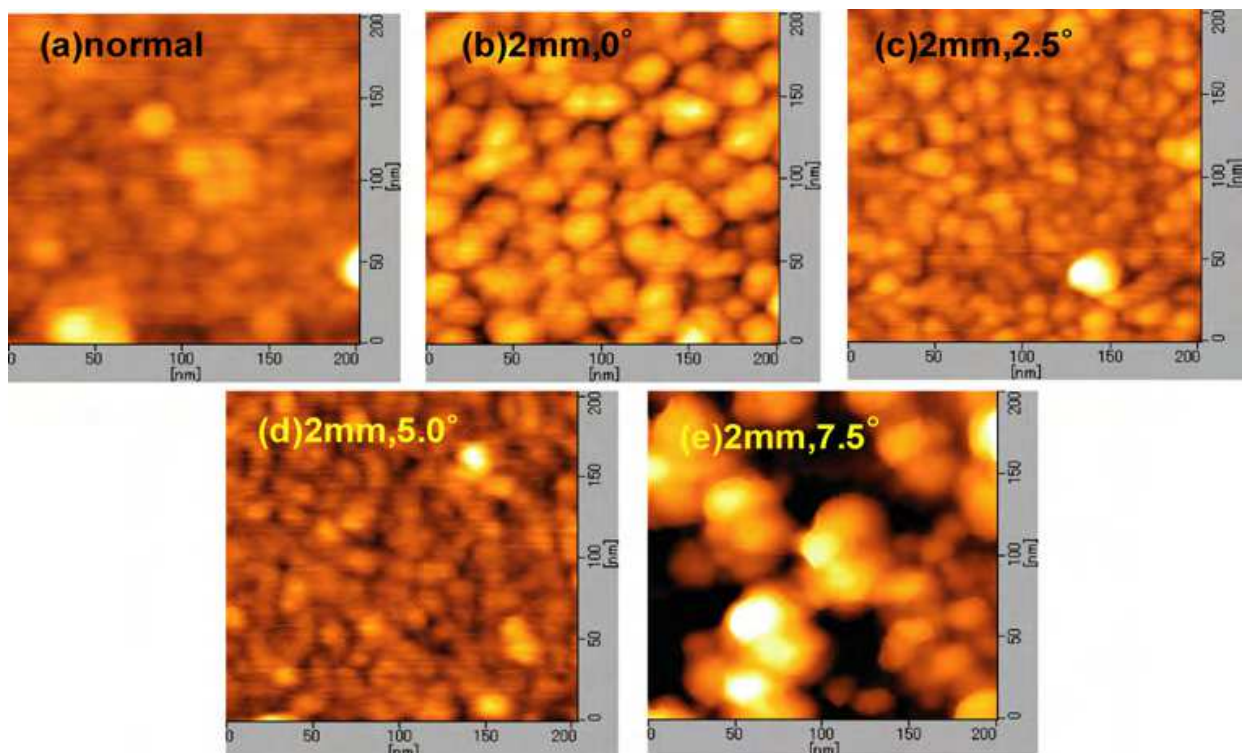
Fig. 13. Influence of shock wave confinement on deposited nanoparticles morphology in the ellipsoidal cell (field of view:200×200nm)

mm, as shown in Figure 13(b), some aggregation is observed. The result in Figure 13(c), where $x$ = 2.0 mm and $\theta$= 2.5°, shows the appearance of fine nanoparticles, similar to the normal case (Figure 13(a)). The mainly small and uniformly sized nanoparticles shown in Figure 13(d) formed under conditions of $x$ = 2.0 mm and $\theta$ = 5.0°. In contrast, when $x$ = 2 mm, $\theta$ = 7.5°, secondary particles were generated by nanoparticle aggregation (Figure 13(e)). Although the position of the laser spot is shifted and also the density of laser energy is slightly changed (Figures 13(c) and 13(d)) relative to the normal case (Figure 13(a)), the sizes of the resulting nanoparticles were found to be finely dispersed, similar to the normal case. The confinement effect of the plume by the converging shock wave plays a role in these cases, because the plume ejection is approximately directed to the focal point of the ellipsoidal cell. The result of Figure 13(e) indicates that the residence time of nanoparticles in the ellipsoidal cell increased due to circulation by a vortex flow resulting from the shifted direction of the plume ejection relative to the focal point.

## 5.4 Low temperature sintering

As mentioned above, nanoparticle size was found to be monodispersed in the ellipsoidal cell under appropriate conditions. We will now discuss a case in which the monodispersed nanoparticles were sintered under low-temperature conditions. This low-temperature sintering procedure could serve as a metal bonding technique.
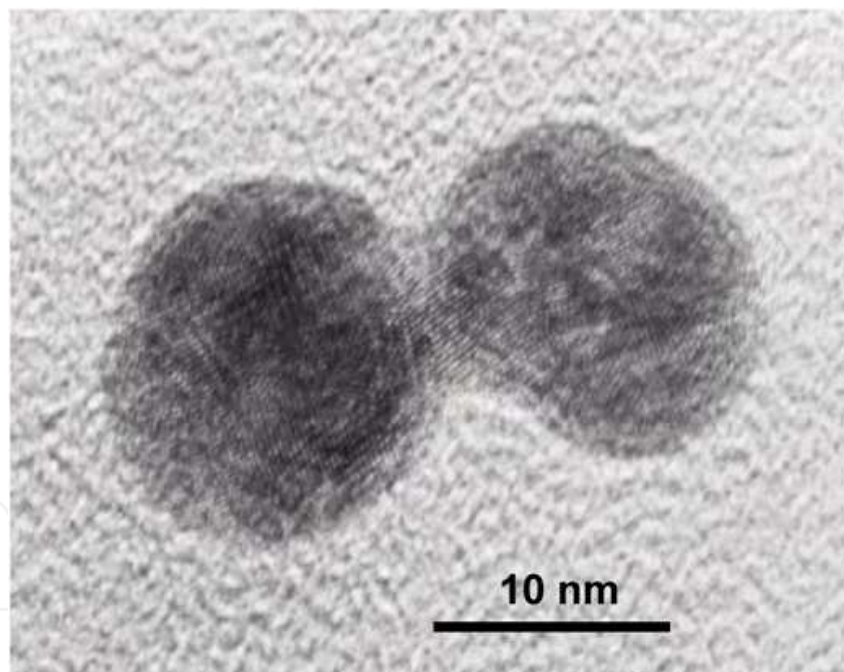


Fig. 14. Two gold nanoparticles forming a neck and binding to each other.

The bonding of metal is an important process for the construction of fine mechanical parts and heat sinks. Conventional bonding methods such as diffusion bonding, melted alloy bonding, hot isostatic pressing and silver brazing cause thermal stress at the interface between two metals because of differences in thermal expansion between the bonded parts. This thermal stress in turn causes warping of the bonded material. Therefore, low-temperature metal bonding is desired to overcome these problems. Since the melting point of metals decreases with decreasing particle size, metal nanoparticle paste has been used as

a low-temperature bonding material. However, the bonding strength of nanoparticle paste is relatively low. Since the sintering of monodispersed nanoparticles has been observed to effectively bond metals, it is important to elucidate this sintering phenomenon in order to optimize the strength of the metal bonding.

The TEM image in Figure 14 shows two gold nanoparticles bonding to each other. In crystallized metallic nanoparticles, bonding between the nanoparticles starts to form even at room temperature if the crystal orientations of the two particles are coincident at the interfaces as shown.

Even if the crystal orientations do not match, it is possible for nanoparticles to bond to each other by using a low-temperature sintering effect which lowers the melting point of the material making up the nanoparticles. In the sintering phenomena of two particles at a certain high temperature, melting, vaporization and diffusion locally occurring in the particle surface result in a fusion at the narrowest neck portion of the contact area between the two particles.

It is well known that the melting point of a substance decreases with decreasing the particle size of materials. The decrement of the melting point, $\Delta T$, for a nanoparticle of diameter $d$ is expressed as follows (Ragone, D. V, 1996):

$$\Delta T = -\frac{4V_s \gamma_{l-s} T_m}{\Delta H_m} \frac{1}{d}$$

(17)

where, $V_s$ is the volume per mole, $\Delta H_m$ is the melting enthalpy per mole, $\gamma_{l-s}$ is the interface tension between the liquid and solid phase, and $\Delta T_m$ is the melting point for the bulk material. If we assume that the material is copper, $\Delta T$ is about 160 K for a copper nanoparticle having a diameter of 10 nm. We also assume that the interface tension, $\gamma_{l-s}$, is half the value of bulk surface tension.

The decrease in the melting point results in a decrease in the sintering temperature and strengthens the diffusion bonding at relatively low temperatures. In general, diffusion bonding is enhanced by the sintering process, in which atomic transport occurs between the small bumps on the material surface. By irradiating nanoparticles onto the surface of the materials before bonding, the number of effective small bumps greatly increases.

In some experiments, the aggregation of the nanoparticles was found to be the smallest when the helium background gas pressure was suitable for the dispersion conditions. AFM images of nanoparticles formed under these conditions by the PLA method show that the size of the nanoparticles ranges from 10 nm to several tens of nm. Annealing at comparatively low temperature was performed on nanoparticles formed under these conditions. Figure 15(a) shows an AFM image of nanoparticles before annealing, and and Figures 15(b), 15(c), and 15(d) show them after annealing at 473 K, 573 K and 673 K, respectively. As can be seen from the images, nanoparticle size increased with annealing temperature.

According to sintering process theory, the final diameter of a nanoparticle, $d_f$, is dependent on the annealing temperature. Particle growth rate can be expressed using the surface area of a nanoparticle by (Koch, W. 1990):

$$\frac{da}{dt} \propto -\frac{1}{\tau}\left(a - a_f\right)$$

(18)

where $t$ is the time, $\tau$ is the characteristic time of particle growth by sintering, $a$ is the surface area, and $a_f$ the value of the surface area at a final size. The particle growth rate is dependent on $\tau$, which is determined by two main types of the diffusion: lattice diffusion and the grain boundary diffusion. The characteristic time of the lattice diffusion, $\tau_l$, is proportionate to the third power of the particle diameter, $d$, and temperature, $T$, and it is inversely proportional to the surface energy, $\gamma$, and the diffusion constant, $D$. Therefore, $\tau_l$ is expressed as (Greer, J. R., 2007)

$$\tau_l \propto \frac{kTd^3}{\gamma D} = \frac{kTd^3}{\gamma D_0}\exp\left(\frac{\varepsilon}{kT}\right) \tag{19}$$

where $k$ is the Boltzman constant, $D_0$ is the vibrational constant, and $\varepsilon$ the activation energy for diffusion. If $\tau$ used in Eq.(18) is known, the final diameter, $d_f$, can be estimated from the correlation between the diameter and annealing time.

As shown in Eq. (19), the characteristic time $\tau_l$ seems to increase proportionally with temperature, but $\tau_l$ actually decreases with increasing temperature due to the large contribution of temperature in the exponential term of the equation. However, the characteristic time $\tau_b$ for grain boundary diffusion is always shorter than $\tau_l$ under low-temperature conditions. As a result, if $\tau_b$ is used as the value of $\tau$ in Eq.(18), the final particle size $d_f$ can be estimated by measuring the particle sizes at specified time intervals.

Since a large $\tau$ value corresponds to an unfavorable degree of the sintering, it is necessary to reduce the value of $\tau$ in order to enhance the sintering process. It can be deduced from Eq. (19) that it is effective to not only increase temperature but also to decrease the diameter of the nanoparticles. From the viewpoint of low-temperature bonding, however, it is preferable to keep the temperature as low as possible and to decrease the size of the nanoparticles before annealing.
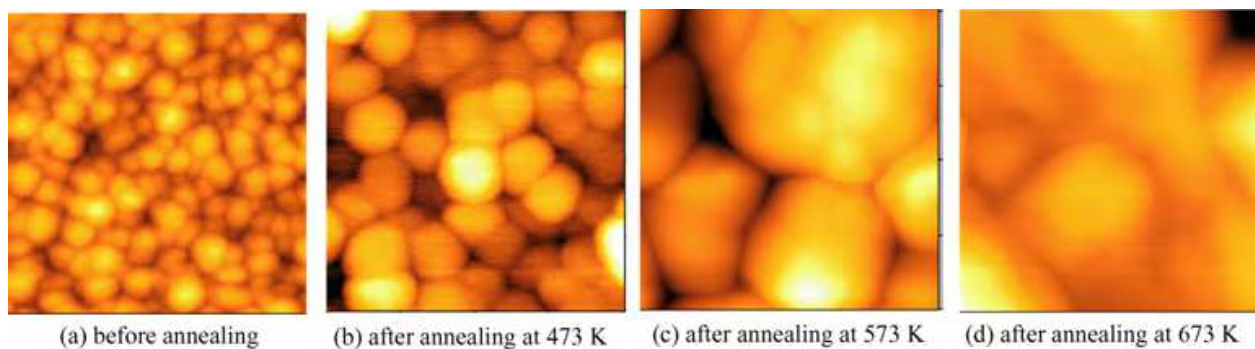


(a) before annealing    (b) after annealing at 473 K    (c) after annealing at 573 K    (d) after annealing at 673 K

Fig. 15. Nanoparticle sintering at various temperatures (field of view:200×200nm).

## 6. Summary

In this chapter, several topics on the thermodynamics of nanoparticles formation under laser ablation were explored.

Firstly, thermodynamics related to some general aspects of nanoparticle formation in the gas phase and the principles behind of pulsed laser ablation (PLA) was explained. We divided the problem into the following parts for simplicity: (i) nanoparticle nucleation and growth, (ii) melting and evaporation by laser irradiation, and (iii) Knudsen layer formation. All these considerations were then used to build a model of nanoparticle formation into fluid dynamics equations.

Secondly, fluid dynamics concerning nanoparticle formation in a high speed flow was developed. Interactions between the shock waves and plume, generation of nuclei, and growth of nanoparticles could all be treated with a single calculation. We conducted one-dimensional calculations with the equation, and found conditions wherein the timing of the nucleation and growth processes could be separated based on interactions between the shock wave and plume. The existence of certain conditions for nanoparticle formation in the narrow region between the plume and the buffer gas were confirmed from the numerical results. In addition, reflected shock waves substantially contribute to the growth of nanoparticles by increasing particle radius, but do not contribute to the increase of nanoparticle numbers by promoting nucleation.

A new model of nanoparticle generator, employing an ellipsoidal cell, was then formulated based on the results of the one-dimensional calculations. To evaluate the performance of the cell, axi-symmetric two-dimensional calculations were conducted using Navier-Stokes equations without nanoparticle formation. The behavior of shock wave and plume became clear with the use of density contour maps. The reflection and conversion of shock waves, the interaction between shock wave and plume, and ejection of gas through the cell exit were clearly illustrated.

The ellipsoidal cell was manufactured and PLA process was experimentally carried out in the cell. Cu nanoparticles formed in the experiment were typically of uniform size, under 10 nm in diameter, and had a narrow size distribution, with a standard deviation around 1.1 for the lognormal distribution. The narrow distribution of nanoparticle size possibly originated from the effect of ellipsoidal cell, because the fine, uniform nano-sized particles could not be obtained unless the direction of plume ejection was coincident with the focal point of the ellipsoidal cell. Such uniformly sized nanoparticles are important for practical use as indicated by the following example.

Finally, the thermodynamics of nanoparticle sintering was explored, in particular the transition of nanoparticle appearance with changes in temperature, as well as the possibility of low temperature bonding. Since the melting point of nanoparticles sensitively depends on size, it is important to prepare uniformly sized nanoparticles for bonding at low temperatures.

## 7. References

AIST Home Page, Research Information Database, Network Database System for Thermophysical Property Data, (2006), http://riodb.ibase.aist.go.jp/TPDB/DBGVsupport/detail/silicon_en.html.

Camata, R. P., Atwater, H. A., Vahala, K. J. and Flagan, R. C. (1996), Size classification of silicon nanocrystals, Appl. Phys. Lett. 68 (22), 3162-3164.

Chrisey, D.B. and Hubler G.K. (Eds.) (1994), Pulsed Laser Deposition of Thin Films, Wiley-Interscience, New York.

Finney, E. E. and Finke, R. G. (2008), Nanocluster nucleation and growth kinetic and mechanistic studies: A review emphasizing transition-metal nanoclusters, Journal of Colloid and Interface Science 317, 351–374.

Fukuoka, H., Yaga, M. and Takiya, T. (2008), Study of Interaction between Unsteady Supersonic Jet and Shock Waves in Elliptical Cell, Journal of Fluid Science and Technology, 3-7, 881-891.

Greer, J. R. and Street, R. A. (2007), Thermal cure effects on electrical performance of nanoparticle silver inks, Acta Mater. 55, 6345-6349.

Han, M., Gong, Y. Zhou, J. Yin, C. Song, F. Muto, M. Takiya T. and Iwata, Y. (2002), Plume dynamics during film and nanoparticles deposition by pulsed laser ablation, Phys. Lett., A302, 182-189.

Houle F. A. and Hinsberg, W. D. (1998), Stochastic simulation of heat flow with application to laser–solid interactions, Appl. Phys., A66, 143-151.

Ide, E., Angata, S., Hirose, A. and Kobayashi, K. (2005), Metal-metal bonding process using Ag metallo-organic nanoparticles, Acta Materialia 53, 2385–2393.

Inada, M., Nakagawa, H., Umezu, I. and Sugimura, A. (2003), Effects of hydrogenation on photoluminescence of Si nanoparticles formed by pulsed laser ablation, Materials Science and Engineering B101, 283-285.

Ito, S., Nakaoka, K., Kawamura, M., Ui, K., Fujimoto, K. and Koura, N. (2005), Lithium battery having a large capacity using $Fe_3O_4$ as a cathode material, Journal of Power Sources 146, 319–322.

Iwata, Y. Kishida, M. Muto, M. Yu, S. Sawada, T. Fukuda, A. Takiya, T. Komura A. and Nakajima, K. (2002), Narrow size-distributed silicon cluster beam generated using a spatiotemporal confined cluster source, Chem. Phys. Lett., 358, 36-42.

Kim, K., Park, J. H., Doo, S. G., Nam, J. D. and Kim, T. (2009), Generation of size and structure controlled Si nanoparticles using pulse plasma for energy devices, Thin Solid Films 517, 4184–4187.

Kim, K., Park, J. H., Doo, S. G. and Kim, T. (2010), Effect of oxidation on Li-ion secondary battery with non-stoichiometric silicon oxide (SiOx) nanoparticles generated in cold plasma, Thin Solid Films 518, 6547–6549.

Knight, C. J. (1979), Theoretical Modeling of Rapid Surface Vaporization with Back Pressure, AIAA J., 17-5, 519-523.

Koch W. and Friedlander S. K. (1990)，The effect of particle coalescence on the surface area of a coagulation aerosol, Journal of Colloid and Interface Science, 140-2, 419.

Li, S. and El-Shall, M. S. (1998), Synthesis of nanoparticles by reactive laser vaporization: silicon nanocrystals in polymers and properties of gallium and tungsten oxides, Applied Surface Science 127–129, 330–338.

Li, Q., Sasaki, T., Koshizaki, N. (1999), Pressure dependence of the morphology and size of cobalt (II,III) oxide nanoparticles prepared by pulsed-laser ablation, Appl. Phys. A 69, 115–118.

Liqiang, J., Xiaojun, S., Jing, S., Weimin, C., Zili, X., Yaoguo, D. and Honggang, F. (2003), Review of surface photovoltage spectra of nanosized semiconductor and its applications in heterogeneous photocatalysis, Solar Energy Materials & Solar Cells 79, 133–151.

Liqiang, J., Baiqi, W., Baifu, X., Shudan, L., Keying, S.,Weimin, C. and Honggang, F. (2004), Investigations on the surface modification of ZnO nanoparticle photocatalyst by depositing Pd, Journal of Solid State Chemistry 177, 4221–4227.

Lu, M., Gong, H., Song, T., Wang, J. P., Zhang, H. W. and Zhou, T. J. (2006), Nanoparticle composites: FePt with wide-band-gap semiconductor, Journal of Magnetism and Magnetic Materials 303, 323–328.

Patrone, L., Nelson, D., Safarov, V.I., Giorgio, S., Sentis, M. and Marine, W. (1999), Synthesis and properties of Si and Ge nanoclusters produced by pulsed laser ablation, Appl. Phys. A 69 [Suppl.], S217–S221.

Patrone, L., Nelson, D., Safarov, V. I., Sentis, M. and Marine, W. (2000), Photoluminescence of silicon nanoclusters with reduced size dispersion produced by laser ablation, Journal of Applied Physics Vol.87, No.8, 3829-3837.

Ragone，D. V. (1996), Chemical physics of materials Ⅱ, Maruzen, (Translated into Japanese).

Roco, M. C. (1998), Reviews of national research programs in nanoparticle and nanotechnology research in the U.S.A., J. Aerosol Sci. Vol. 29, No. 5/6, pp. 749-760.

Seto, T., Koga, K., Takano, F., Akinaga, H., Orii, T., Hirasawa, M. and Murayama, M. (2006), Synthesis of magnetic $CoPt/SiO_2$ nano-composite by pulsed laser ablation, Journal of Photochemistry and Photobiology A: Chemistry 182, 342–345.

Shapiro, A. H. (1953) The Dynamics and Thermodynamics of COMPRESSIBLE FLUID FLOW, Ronald Press, New York.

Strickland, N. M., Long, N. J., Talantsev, E. F., Hoefakker, P., Xia, J. A., Rupich, M. W., Zhang, W., Li, X., Kodenkandath, T. and Huang, Y. (2008), Nanoparticle additions for enhanced flux pinning in YBCO HTS films, Current Applied Physics 8, 372–375.

Suzuki, N., Makino, T., Yamada, Y. and Yoshida, T. (2001), Monodispersed, nonagglomerated silicon nanocrystallites, Applied Physics Letters, Vol.78, No.14 , 2043-2045.

Takiya, T., Umezu, I., Yaga, M. and Han, M. (2007), Nanoparticle Formation in the Expansion Process of a Laser Ablated Plume, J. Phys. Conf. Ser. 59, 445.

Takiya, T., Fukuda, N., Inoue, N., Han, M., Yaga, M. and Iwata, Y. (2010), Dynamics of the Shock Wave Accompanied by Nanoparticle Formation in the PLA Processes, Adv. Studies Theor. Phys., Vol. 4, no.7, 305 – 316.

Touloukian, Y. S., editor. (1967), Thermophysical Properties of High Temperature Solid Materials, The Macmillan Co., New York.

Volmer, M. (1939), Kinetik der Phasenbildung, T. Steinkopff, Dresden, Leipzig.

Weast, R. C., editor. (1965), Handbook of Chemistry and Physics 46th edition, The Chemical Rubber Co., Ohio.

Wegner, K., Piseri, P., Tafreshi H. V. and Milani, P. (2006), Cluster beam deposition: a tool for nanoscale science and technology, J. Phys. D: Appl. Phys. 39, R439–R459.

Wu, H. P., Okano, A. and Takayanagi, K. (2000), Photoluminescence properties of size-selected Si nanocluster films prepared by laser ablation, Appl. Phys. A 71, 643–646.

Yaga, M. Takiya T. and Iwata, Y. (2005), Numerical study of unsteady compressible flow driven by supersonic jet injected into ellipsoidal cell with small exit hole, Shock waves, 14-5/6, 403-411.

Yaga, M., Fukuoka, H., Iwata, Y. and Takiya, T. (2008), Behavior of Shock Waves Formed by Unsteady Supersonic Jet Injected into Cell, Journal of Thermal Science, 17-1, pp.50-55.
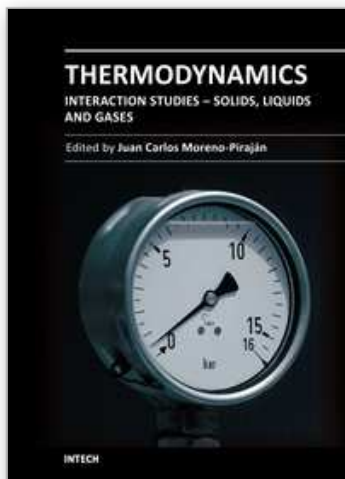
**Thermodynamics - Interaction Studies - Solids, Liquids and Gases**
Edited by Dr. Juan Carlos Moreno Piraján

Thermodynamics is one of the most exciting branches of physical chemistry which has greatly contributed to the modern science. Being concentrated on a wide range of applications of thermodynamics, this book gathers a series of contributions by the finest scientists in the world, gathered in an orderly manner. It can be used in post-graduate courses for students and as a reference book, as it is written in a language pleasing to the reader. It can also serve as a reference material for researchers to whom the thermodynamics is one of the area of interest.

**How to reference**
In order to correctly reference this scholarly work, feel free to copy and paste the following:

# INTECH
open science | open minds